ACS APPLIED MATERIALS & INTERFACES

www.acsami.org

Research Article

All-Oxide p−n Junction Thermoelectric Generator Based on SnO_x and ZnO Thin Films

Eliana M. F. Vieira,* José P. B. Silva,* Kateřina Veltruská, Cosmin M. Istrate, Veniero Lenzi, Vanira Trifiletti, Bruno Lorenzi, Vladimír Matolín, Corneliu Ghica, Luis Marques, Oliver Fenwick, and Luis M. Goncalves

Cite This: *ACS Appl. Mater. Interfaces* 2021, 13, 35187−35196

Read Online

ACCESS | Metrics & More | Article Recommendations | Supporting Information

ABSTRACT: Achieving thermoelectric devices with high performance based on low-cost and nontoxic materials is extremely challenging. Moreover, as we move toward an Internet-of-Things society, a miniaturized local power source such as a thermoelectric generator (TEG) is desired to power increasing numbers of wireless sensors. Therefore, in this work, an all-oxide p−n junction TEG composed of low-cost, abundant, and nontoxic materials, such as n-type ZnO and p-type SnO_x thin films, deposited on borosilicate glass substrate is proposed. A type II heterojunction between SnO_x and ZnO films was predicted by density functional theory (DFT) calculations and confirmed experimentally by X-ray photoelectron spectroscopy (XPS). Moreover, scanning transmission electron microscopy (STEM) combined with energy-dispersive X-ray spectroscopy (EDS) show a sharp interface between the SnO_x and ZnO layers, confirming the high quality of the p−n junction even after annealing at 523 K. ZnO and SnO_x thin films exhibit Seebeck coefficients (α) of ∼121 and ∼258 μV/K, respectively, at 298 K, resulting in power factors (PF) of 180 μW/m K^2 (for ZnO) and 37 μW/m K^2 (for SnO_x). Moreover, the thermal conductivities of ZnO and SnO_x films are 8.7 and 1.24 W/m K, respectively, at 298 K, with no significant changes until 575 K. The four pairs all-oxide TEG generated a maximum power output (P_{out}) of 1.8 nW (≈126 μW/cm^2) at a temperature difference of 160 K. The output voltage (V_{out}) and output current (I_{out}) at the maximum power output of the TEG are 124 mV and 0.0146 μA, respectively. This work paves the way for achieving a high-performance TEG device based on oxide thin films.

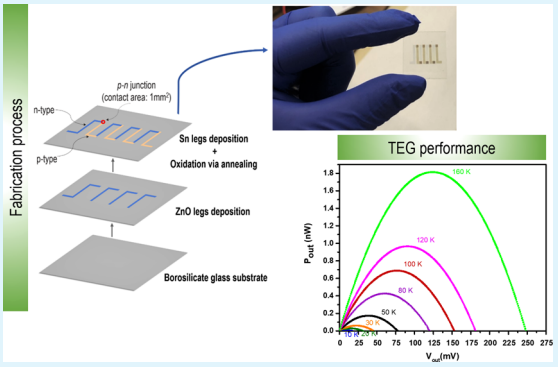

KEYWORDS: *thermoelectricity, energy generation, all-oxide device, p−n junction, density functional theory, TEGs*

INTRODUCTION

Thermoelectric generators (TEGs) are devices with the capability to convert waste heat into electrical energy. The maximum efficiency of the thermoelectric (TE) energy conversion is related to the figure-of-merit, $ZT = \alpha^2\sigma/k(T)$ of the TE materials, whereby α is the Seebeck coefficient, σ is the electrical conductivity, and k is the thermal conductivity, at a specific temperature T and also depends on the device design.[1,2] Several strategies have been undertaken to improve the performance of TE devices over the past several decades,[3,4] but it is still problematic to achieve high ZT values without the use of scarce and high-cost materials (such as Bi, Te, and Sb). In our recent work, a p−n junction TEG device based on Bi_2Te_3 and Sb_2Te_3 thin films was developed with good thermoelectric performance (3.3 mW/cm^2 of density power),[5] but the cost is too high for large exploitation and their practical utilization is limited due to a near-room temperature (RT) operating range. In addition, these devices seem to be unstable at high temperatures and tend to have oxidation issues.[6] Therefore, it is important to fabricate a low-priced device, with more abundant and eco-friendly materials, as this can be more powerful than to have a very high-performance TEG with an unpredictable price. To provide good efficiency while reducing the use of expensive and rare materials, researchers have developed TE devices using inorganic compounds−organic polymers due to their low-cost processing, biocompatibility, and flexibility.[6,7] In this context, we highlighted the work developed by Pires et al.[6] with a TEG made by 10 legs of Bi_2Te_3−poly(vinyl alcohol) (PVA) thick inks with a power output of ∼9 μW/cm^2 for a small temperature gradient of 46 K. Moreover, high power densities of more than 10 μW/cm^2 have also been recently reported involving Te-nanorod−

Received: May 26, 2021
Accepted: June 29, 2021
Published: July 13, 2021

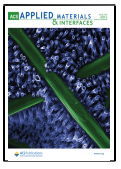

Table 1. Performance of All-Oxide p−n Thermoelectric Generators with Different Material Systems and Device Configurations[a]

TE units	type of construction	no. of pairs	ΔT (K)	output power, P_{out}	references
p-Li-doped NiO; n-(Ba, Sr)PbO_3	vertical	4	539	34.4 mW	Shin et al.[46]
p-$Ca_{2.75}Gd_{0.25}Co_4O_9$; n-$Ca_{0.92}La_{0.08}MnO_3$	vertical	8	390	21 mW/cm^2	Matsubara et al.[1111]
p-$Ca_{0.76}Cu_{0.24}Co_4O_9$; n-$Ca_{0.8}Dy_{0.2}MnO_3$	vertical	4	346	8.42 mW	Park et al.[47]
p-ZnO; n-CuO	longitudinal (2D layered)	5		1 nW/(K^2 m^2)	Zappa et al.[48]
p-$Ca_3Co_{4-x}O_{9+\delta}$; n-$CaMnO_{3-\delta}$−$CaMn_2O$	vertical	1	160	5.7 mW 23 mW/cm^2	Kanas et al.[49]
p-$Ca_2Co_2O_5$; n-TiO_{2-x}	longitudinal (2D layered)	1	450	0.2 mW/cm^2	Caliari et al.[50]
p-$Ca_3Co_{4-x}O_{9+\delta}$; n-$CaMnO_{3-\delta}$−$CaMn_2O_4$	vertical	1	650	7.2 mW 28.9 mW/cm^2	Kanas et al.[51]
p-SnO_x; n-ZnO	planar	4	160	1.8 nW 126 μW/cm^2	this work

[a]The performance of the TEG presented in this work is also shown.

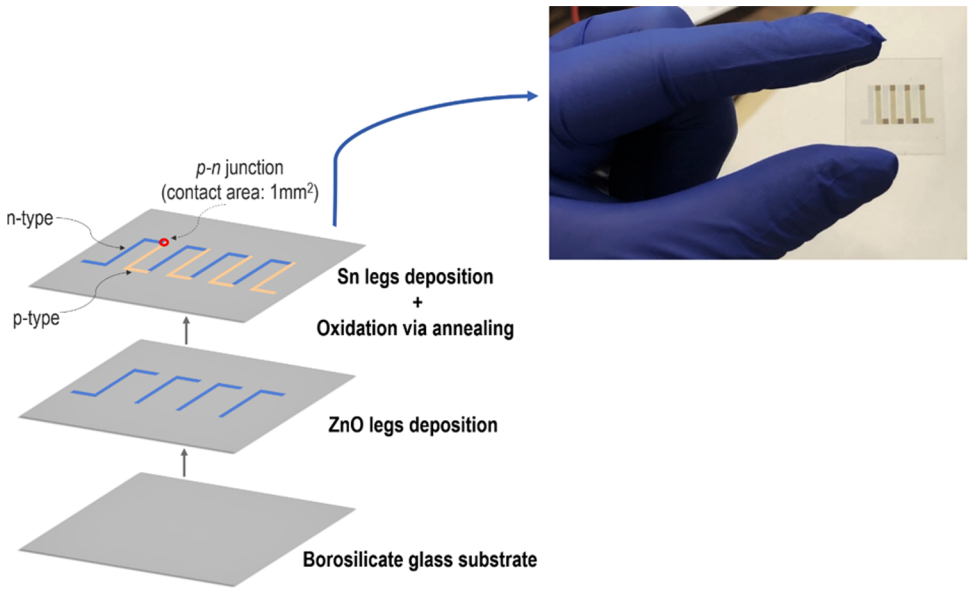

Figure 1. (Left) Schematic describing the fabrication process of the p−n TEG and (right) photograph of the developed thin-film TEG showing a good overlapping of the well-defined n- and p-legs.

poly(3,4-ethylenedioxythiophene):polystyrene sulfonate (PEDOT:PSS)[8] and Cu_2Se−PEDOT:PSS composite materials.[9] In turn, Park et al.[10] reported a TE device made by only four pairs of ZnO/Al_2O_3−$Bi_{0.5}Sb_{1.5}Te_3$ legs that generated ∼1 nW at ΔT = 80 K. However, these devices still have a high cost due to the presence of tellurium alloys.

Therefore, all-oxide TE devices for energy harvesting are promising due to their cost-effectiveness, the use of earth-abundant and nontoxic elements, and their stability in oxidizing atmospheres over a wide range of operating temperatures.[11] Table 1 summarizes the TE performance of some examples of all-oxide p−n TE generators employing different material systems and TEG configurations. The performance of the TEG presented in this work is also shown. It is noted that the TE devices with a vertical configuration can generate higher power density levels (in the range of mW/cm^2), mainly due to the higher cross-sectional area of the thermoelectric legs. These devices are composed of bulky elements (of several microns or few millimetres) to sustain higher temperature differences (ΔT), which limits their integration in micro/nano-electromechanical systems, such as smart watches, fitness trackers, wireless networks, and biomedical devices (e.g., health monitoring devices adapted to the human body).[12−14] In this context, a two-dimensional (2D) layered configuration has a higher potential for integration in micro/nano-engineering structures, with the advantage that it can be designed to output large voltages at relatively small ΔT.[15] Moreover, using TE thin films, the devices can benefit from small size and low weight.

Therefore, in this work, a prototype of an all-oxide 2D thin-film TEG was performed with four n-ZnO and p-SnO_x pairs. The junctions between the oxide materials are formed where they overlap one another, which eliminates the need for external connecting electrodes and therefore the energy losses

https://doi.org/10.1021/acsami.1c09748
ACS Appl. Mater. Interfaces 2021, 13, 35187−35196

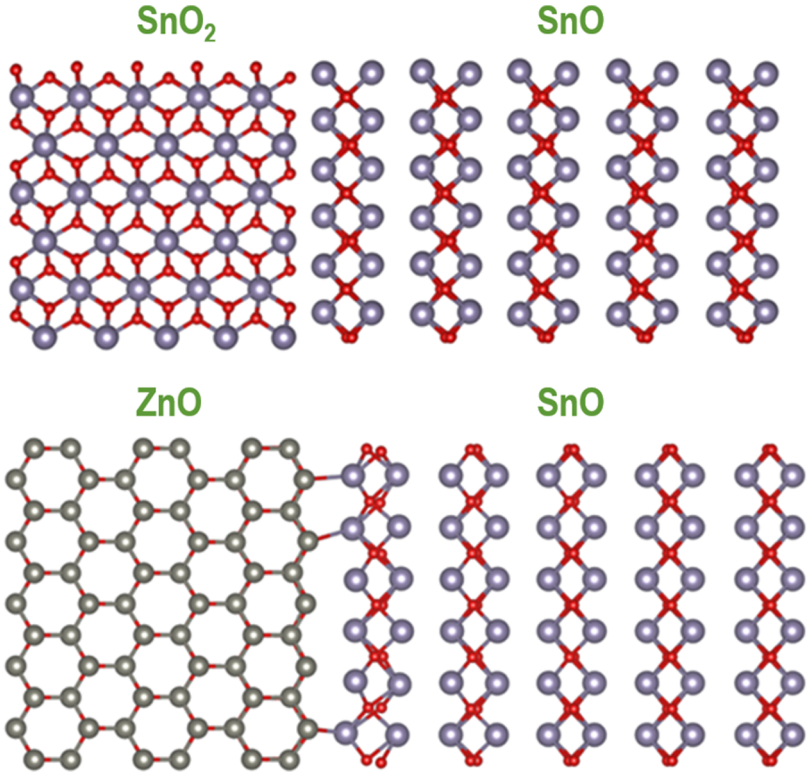

Figure 2. Optimized SnO_2/SnO (top) and ZnO/SnO (bottom) interfaces, as seen from an in-plane direction. In the representations, gray spheres are Zn atoms, red ones are O atoms, and light purple ones are Sn atoms.

via the contact resistance. We decided to use n-type ZnO films owing to their promising TE properties over a wide temperature range (RT to 1300 K).[16] On the other hand, we decided to use p-SnO_x since we have shown that p-type tin oxide (SnO_x) thin films can exhibit high thermoelectric performance, especially due to their high Seebeck coefficients.[17] The interface structure and band alignment of the ZnO/SnO_x heterojunction were investigated by scanning transmission electron microscopy (STEM) and X-ray photoelectron spectroscopy (XPS) experiments correlated with density functional theory (DFT) calculations, which provide evidence of the formation of a type II heterojunction. The thermoelectric characteristics of the individual n-ZnO and p-SnO_x materials were investigated and associated with the TEG performance.

MATERIALS AND METHODS

Fabrication of Thin Films. A transparent ∼110 nm thick ZnO film used for a n-type thermoelectric leg was fabricated by pulsed laser deposition (PLD). The film was fabricated on borosilicate glass (20 mm × 20 mm) using a commercial ZnO target (99.99% purity from Kurt Lesker). The substrate was held at 673 K, at an oxygen partial pressure of 0.01 mbar. The 248 nm line of an excimer laser, with energy of 400 mJ and pulse rate of 10 Hz, was focused on the target. The p-type film was achieved by the thermal evaporation of a metallic Sn thin film and further annealing in air at 523 K for 3 h, with a heating/cooling rate of 278 K/min, obtaining a 70 nm thick SnO_x thin film. The thickness of the SnO_x films was 70 nm to ensure that the films had the best TE and electric properties and to maximize the output power density of the TEG. These parameters are critically dependent on the thickness of the SnO_x layer and annealing parameters, as we demonstrated in our recent work.[17] The deposition parameters were investigated to optimize the TE and electric properties of the ZnO films. Thin films were characterized in isolation prior to TEG characterization.

Device Fabrication. The TEG device was fabricated using laser cut patterned stainless steel shadow masks to pattern L-shaped strips (8 mm (length) × 1 mm (width)) on top of a borosilicate glass substrate. The TEG consists of four pairs of ZnO−SnO_x legs, in which each film was fabricated using the experimental parameters described above. The ZnO layers were deposited by PLD before the deposition of the SnO_x layers on top due to the higher-temperature fabrication. After the Sn deposition by thermal evaporation, the whole TEG structure (ZnO layers + Sn layers) was annealed in air at 523 K for 3 h to promote Sn oxidation. The fabrication steps are summarized in Figure 1.

Thin Film Characterization. TEM images of the p−n heterojunction device were obtained on a JEM-ARM 200F analytical electron microscope operated at 200 kV. The details of sample preparation can be found elsewhere.[18] X-ray photoelectron spectroscopy (XPS) measurements were carried out using the experimental conditions that can be found in ref 14. In-plane Seebeck coefficients, α, of ZnO and SnO_x films were measured at 298 K in the "two-probe" configuration.[19] Each film was connected at two metal blocks with two Pt-100 sensors, and a small thermal gradient was generated along the filmby the Yokogawa source model 7651 equipment. The ΔV was measured by Agilent 34410A 61/2 Digit Multimeter. α values and errors were obtained with the LINEST function, which calculates the statistics for a linear fit using the "least squares" method to calculate the best fit and returns an array that describes the line (slope and error, for example). Seebeck calibration with a standard pure metal (Cu) was performed. Electrical conductivity, σ, measurements were performed using the conventional van der Pauw method. The in-plane thermal conductivities of the oxide films were obtained on films deposited on a suspended Si_3N_4 membrane by a pseudo-steady-state 3-ω method using a Linseis thin film analyzer (described elsewhere[20−22]).

Device Characterization. The thermoelectric power output of the four p−n junction TEGs was measured using a homemade testing system composed of thermoelectric modules (TEC1-12706 model) to create different temperature gradients on the hot and cold sides of the TEG, K-type thermocouples, aluminium heatsinks, and the Optris PI

https://doi.org/10.1021/acsami.1c09748
ACS Appl. Mater. Interfaces 2021, 13, 35187−35196

450 infrared (IR) camera to measure the temperatures. The TEG was placed in between the TE modules. The output voltage (V_{out}), output current (I_{out}), and power output of the TEG are acquired while a known load resistance (R_{load}) is connected to the output terminals of the device. V_{out} and I_{out} values were obtained using an Agilent multimeter model 34410A with $6^{1/2}$ digits. Detailed information on the measurement setup can be found in ref 5.

Computational Details. All ab initio calculations were performed using the projector augmented wave (PAW) method as implemented in the Vienna Ab Initio Simulation Package (VASP), version 5.4.4.[23,24] PAW[25] pseudopotentials were used in all calculations; for Sn and Zn, the semicore s states were treated as valence ones. DFT calculations were employed using the generalized gradient approximation (GGA) approximation and Perdew–Burke–Ernzerhof (PBE) functional.[26] The band offsets were estimated using the ionization potentials (IP) of the materials under consideration.[27,28] The IP was obtained as a difference between the vacuum energy and the Fermi energy

$$\mathrm{IP} = \Delta E_{\mathrm{vac-ref}} - \Delta E_{\mathrm{VBM-ref}} \quad (1)$$

where $\Delta E_{\mathrm{vac\text{-}ref}}$ is the difference between the value of the electrostatic potential far from the surface and its reference value taken in a bulk-like region. $\Delta E_{\mathrm{VBM\text{-}ref}}$ is the difference between the valence band maximum (VBM) obtained from a bulk calculation and the electrostatic potential reference value. The latter is the average of the local Kohn–Sham potential within a PAW sphere over atomic sites in the bulk or in a bulk-like region in slabs. Once the IP is known, the conduction band minimum (CBM) could be obtained by adding the band gap value E_{Gap}

$$E_{\mathrm{CBM}} = E_{\mathrm{VBM}} + E_{\mathrm{Gap}} \quad (2)$$

where the band gap is obtained from bulk calculations and E_{VBM} is the negative of IP.

To obtain the VBM energies and band gaps, the EGW0 approximation to the many-body perturbation theory was employed.[29,30] Initially, unit cells of bulk ZnO, SnO, and SnO_2 were fully relaxed at the PBE level of theory, using a plane wave energy cutoff of 800 eV and a 6 × 6 × 6 γ-centered k-point grid. The lattice parameters were then reset to their experimental values. After this, the GW calculation has been performed using the same k-point grid and plane wave energy cutoff, and a cutoff of 200 eV was employed for the response function. Corrections to the quasiparticle energies due to basis set incompleteness were calculated using a 3 × 3 × 3 k-point grid and added to the 6 × 6 × 6 calculation.[31]

To obtain the vacuum energies, 2 nm thick slabs of SnO, SnO_2, and ZnO, with a vacuum layer of 15 nm were considered. A γ-centered 6 × 6 × 1 k-point grid was employed. The lattice parameters of the dimensions parallel to the surface were kept fixed to their experimental values and the slabs were relaxed until all atomic forces were smaller than 10 meV/Å. By defining the z-axis as the surface normal, the vacuum energy was calculated as the value of the electrostatic potential $\varphi(z)$ averaged over the xy-plane in the vacuum region. It was verified, for all slabs, that the vacuum was thick enough to ensure the convergence of $\varphi(z)$. Only nonpolar surfaces were considered.

To include the interface effects, we also performed explicit interface calculations for the ZnO(1010)/SnO(001) and SnO_2(001)/SnO-(001) heterojunctions, which are represented in Figure 2, to calculate the natural band offset using the approach of Hinuma and collaborators[27]

$$\Delta E_{\mathrm{VBM}}^{A-B} = (\Delta E_{\mathrm{VBM-ref.}A}^{A} - \Delta E_{\mathrm{Vac-ref.}A}^{A} + \Delta E_{\mathrm{Vac-ref.}X}^{A}) + \Delta E_{\mathrm{ref.}X}^{A-B} - (\Delta E_{\mathrm{VBM-ref.B}}^{\mathrm{B}} - \Delta E_{\mathrm{Vac-ref.B}}^{\mathrm{B}} + \Delta E_{\mathrm{Vac-ref.}X}^{\mathrm{B}}) \quad (3)$$

where the subscript A, B, or X indicates that the experimental in-plane lattice constant of material A, B, or their average X was used, and $\Delta E_{\mathrm{ref.}X}^{A-B}$ is the difference in the reference energies between the materials A and B, obtained from bulk-like regions far from the surfaces and the interface.

The plane wave energy cutoff was set to 520 eV for both interfaces. In the ZnO(1010)/SnO(001) case, it was possible to obtain a near-zero lattice mismatch by considering a larger supercell comprising 240 atoms. Conversely, the SnO_2(001)/SnO(001) interface presents a large lattice mismatch of 20%, which was reduced to 12% by considering a SnO cell rotated by 45°. The interfaces were relaxed until forces converged to 10 meV/Å, using a 2 × 2 × 1 and a 4 × 4 × 1 k-point grid for ZnO/SnO and SnO_2/SnO systems, respectively.

RESULTS AND DISCUSSION

Theoretical ab initio calculations were employed to understand which type of junction could be formed between ZnO and

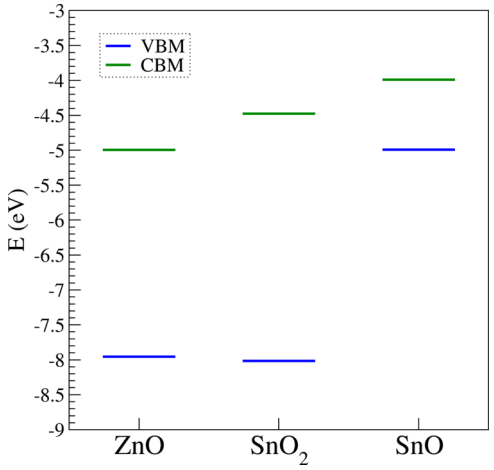

Figure 3. Band alignment between ZnO, SnO_2, and SnO calculated using the EGW0 method. In all pictures, the zero of the energy corresponds to the vacuum energy, as obtained from slab calculations.

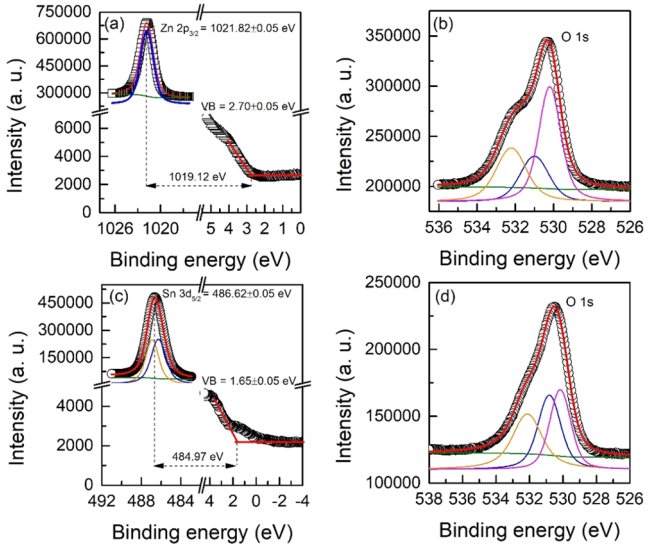

Figure 4. XPS spectra of (a) Zn 2p and the VB region, (b) O 1s for the ZnO film, (c) Sn 3d and the VB region, and (d) O 1s for the SnO_x film.

SnO_x. To treat the problem using DFT, we approximate SnO_x as a polycrystalline SnO_2/SnO system. This way, the relevant p–n interfaces are SnO/SnO_2 and SnO/ZnO. Moreover, pure ZnO, SnO, and SnO_2 materials were employed, i.e., the presence of bulk and/or interfacial defects has been neglected. In Figure 3, we summarize the band alignment as obtained considering the IP of the bulk materials. The ionization

https://doi.org/10.1021/acsami.1c09748
ACS Appl. Mater. Interfaces 2021, 13, 35187–35196

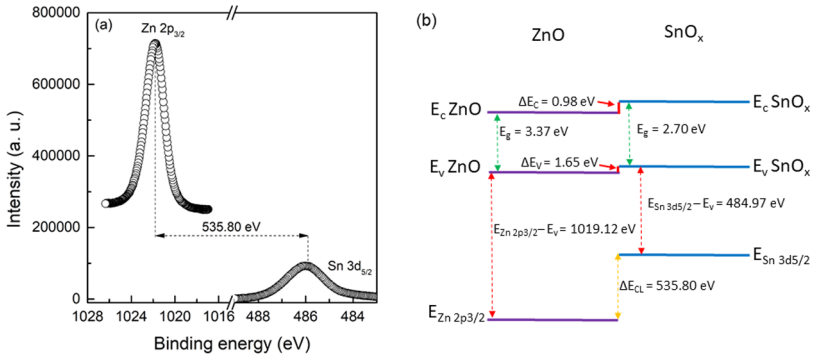

Figure 5. XPS spectra of (a) Sn $3d_{5/2}$ and Zn $2p_{3/2}$ for the SnO_x/ZnO heterojunction. (b) Energy band diagram of the SnO_x/ZnO heterojunction obtained from XPS measurements.

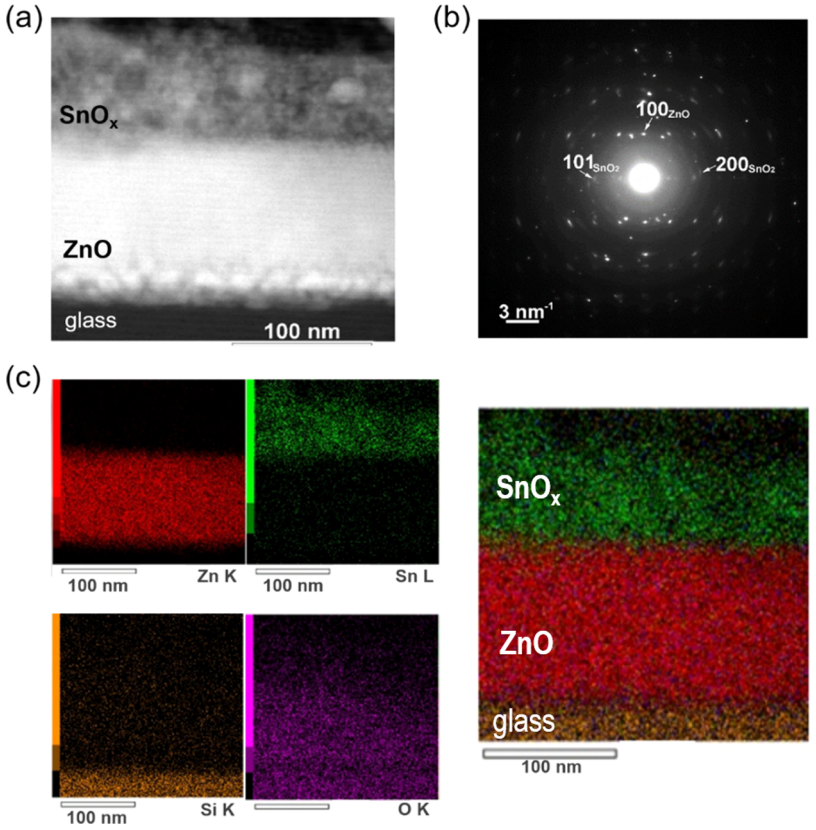

Figure 6. (a) HAADF-STEM image at a low-magnification of the borosilicate glass/n-ZnO/p-SnO_x heterojunction with (b) the corresponding SAED pattern. (c) EDS maps showing the elemental distribution (Zn, red; Sn, green; Si, orange; O, purple). RGB map was obtained by overlapping the Zn, Sn, and Si maps.

potential, IP, of ZnO was found to be 7.96 eV, and its band gap was 2.97 eV, providing a slight underestimation of the experimental value of 3.3 eV.[32] For SnO and SnO_2, we found IPs of 4.99 and 8.01 eV, respectively, with band gaps of 0.99 and 3.54 eV, respectively. It should be noted that SnO is an indirect band gap material, and we report here the indirect gap. These results agree with experimental and theoretical values reported in the literature for SnO_2 and ZnO,[33] whereas for SnO, we found a slight deviation from the experimental values, which are ∼5.7 eV for IP and ∼2.7 eV for the direct gap.[34] Concerning the indirect gap, theoretical calculations performed with hybrid functionals yielded a value of 0.7 eV and a VBM of 4.4 eV.[35]

Regarding the alignment, both the SnO/ZnO and SnO/SnO_2 p−n junctions show a type II behavior. The energy differences in VBM are large for both junctions, around 3 eV, whereas we observe a difference in conduction bands of 0.5 eV for the ZnO/SnO junction and 1.0 eV for the SnO/SnO_2 one.

The natural band offsets obtained using the interface calculations show a slightly different picture: the SnO/SnO_2 offset was 2.99 eV, while the value of 2.09 eV was found for the ZnO/SnO interface. The SnO_2/SnO prediction is in line with the results of Figure 3, while the ZnO/SnO prediction is slightly lower. In both cases, the prediction of a type II heterojunction holds, with the CBM energy differences of 0.12 eV for ZnO/SnO and 0.44 eV for SnO_2/SnO.

Figure 4a,b shows the typical core-level (CL) spectra of the Zn $2p_{3/2}$, valence band (VB) maximum, and O 1s for the ZnO film, respectively. The typical CL spectra of the Sn $3d_{5/2}$, VB, and O 1s for the SnO_x film are shown in Figure 4c,d

https://doi.org/10.1021/acsami.1c09748
ACS Appl. Mater. Interfaces 2021, 13, 35187−35196

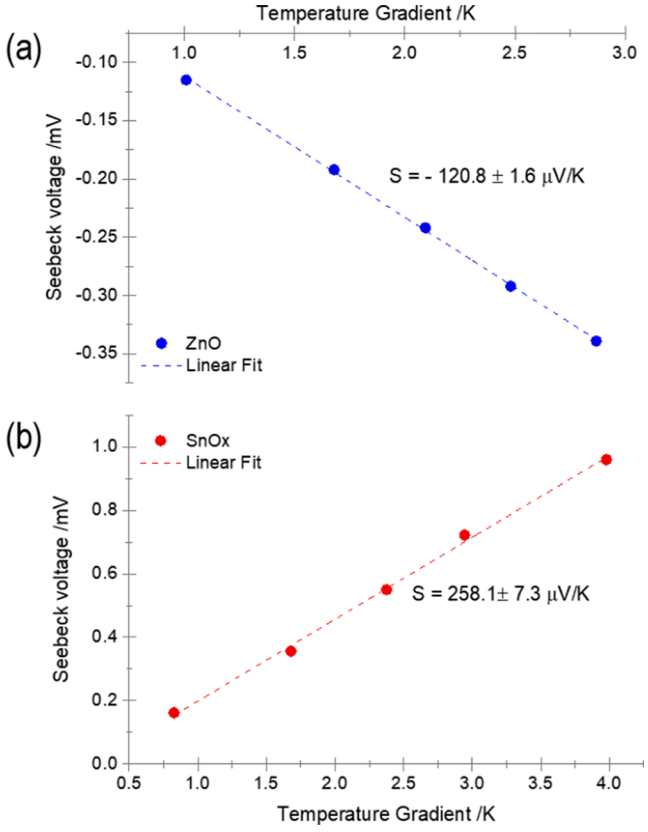

Figure 7. Seebeck voltage measured as a function of the temperature difference applied in the ZnO and SnO_x films. *S* values obtained from the slopes are included.

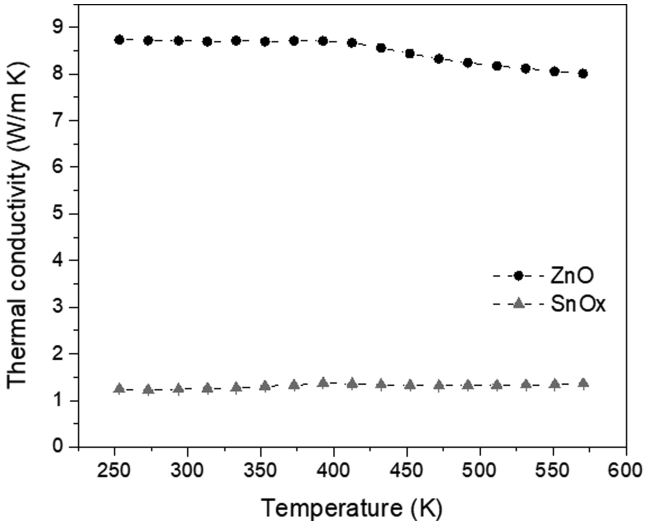

Figure 8. Thermal conductivity of the ZnO and SnO_x thin films deposited on Si_3N_4 membranes.

respectively. The XPS spectra were investigated by fitting the Shirley-type function and a sum of Voigt functions to the experimental results, with the KolXPD software.[29] Only one valence state of Zn is observed at 1021.82 ± 0.05 eV, while the VB value of ZnO is determined to be 2.70 ± 0.05 eV (Figure 4a). The O 1s peak is deconvoluted into three peaks, at 530.19 eV (O^{2-} ions in the ZnO lattice), 531.00 eV (O^{2-} ions in oxygen-deficient regions within the ZnO matrix), and 532.25 eV (chemisorbed and dissociated oxygen species or OH), respectively.[30] Figure 4c shows the fitted Sn $3d_{5/2}$ core-level spectrum with Sn^{2+} (at 486.25 ± 0.05 eV) and Sn^{4+} (at 486.90 ± 0.05 eV) components, respectively, which are in agreement with the reported values.[18] The VB value of SnO_x is determined to be 1.65 ± 0.05 eV. The O 1s peak is deconvoluted into three peaks at 530.16 ± 0.051 eV (associated with $O-Sn^{2+}$), 530.80 ± 0.05 eV (associated with $O-Sn^{4+}$), and 532.13 ± 0.05 eV (absorbed O_x ions), as shown in Figure 4d.[20] The contents of SnO_2 and SnO were calculated using the Sn 3d spectra and were 48 and 52%, respectively, which suggest a p-type SnO_x film.[18] This result is also in good agreement with our previous X-ray diffraction (XRD) studies that confirmed the presence of both phases.[18] Heterostructures can be classified into three types, i.e., type I (symmetric), type II (staggered), or type III (broken).[36] The efficiency of electron–hole pairs splitting at the interface, with electrons transferred to one layer and the holes to the other, is strongly dependent on the heterostructure band alignment architecture.

Therefore, the band alignment at a SnO_x/ZnO interface was investigated by XPS using CL spectra of Sn $3d_{5/2}$ and Zn $2p_{3/2}$ from a very thin SnO_x layer, 2 nm, deposited on top of the ZnO layer, 110 nm (Figure 5a). The ΔE_V at the SnO_x/ZnO interface was determined with the following equation[34,35]

$$\begin{aligned}\Delta E_V &= \Delta E_V \\ &= (E^{SnO_x}_{Sn\ 3d_{5/2}} - E^{SnO_x}_{VB})^{SnO_x} - (E^{ZnO}_{Zn\ 2p_{3/2}} - E^{ZnO}_{VB})^{ZnO} \\ &\quad + (E^{ZnO}_{Zn\ 2p_{3/2}} - E^{SnO_x}_{Sn\ 3d_{5/2}})^{SnO_x/ZnO} \end{aligned} \quad (4)$$

where $(E^{ZnO}_{Zn\ 2p_{3/2}} - E^{SnO_x}_{Sn\ 3d\ 5/2})^{SnO_x/ZnO}$ is the energy difference between Zn $2p_{3/2}$ and Sn $3d_{5/2}$ CLs, while $(E^{SnO_x}_{Sn\ 3d_{5/2}} - E^{SnO_x}_{VB})^{SnO_x}$ and $(E^{ZnO}_{Zn\ 2p_{3/2}} - E^{ZnO}_{VB})^{ZnO}$ are the VB energies with reference to the CL positions of thick SnO_x and ZnO layers, respectively. As shown in Figure 5b, the ΔE_V was found to be 1.65 eV, in reasonable agreement with interface calculations that predict a value of 2.09 eV for the ZnO/SnO interface. The decreased value for ΔE_V is related to the formation of a ZnO/SnO_2 heterojunction, as Figure 3 suggests, since the SnO_x film is composed of SnO and SnO_2. The ΔE_C at the interface was also determined from the following equation[34,35]

$$\Delta E_C = \Delta E_V + E_g^{SnOx} - E_g^{ZnO} \quad (5)$$

where $E_g^{SnO_x}$ and E_g^{ZnO} are the band gap values obtained experimentally for the SnO_x (E_g = 2.70 eV)[18] and ZnO (E_g = 3.37 eV)[37] films, which agrees with the calculated ones. The ΔE_C is 0.98 eV. Figure 5b shows the energy band diagram for the heterojunction, which forms a type II heterostructure, as predicted by DFT calculations. Figure 6a,b shows the high-angle annular dark-field (HAADF)-STEM image of the n-ZnO/p-SnO_x heterojunction and the corresponding electron diffraction (selected area electron diffraction (SAED)) pattern confirming the existence of both deposited layers, where the main diffraction rings can be indexed as the characteristic rings of the ZnO hexagonal phases and the SnO_2 tetragonal rutile phase, respectively. Although there are no diffraction rings related to the SnO phase, probably due to their small concentration, we have unequivocally identified the presence of SnO in the SnO_x layer in the band alignment studies performed by XPS measurements as well as in the deconvolved Sn $3d_{5/2}$ peaks. Furthermore, our previous XRD studies

https://doi.org/10.1021/acsami.1c09748
ACS Appl. Mater. Interfaces 2021, 13, 35187−35196

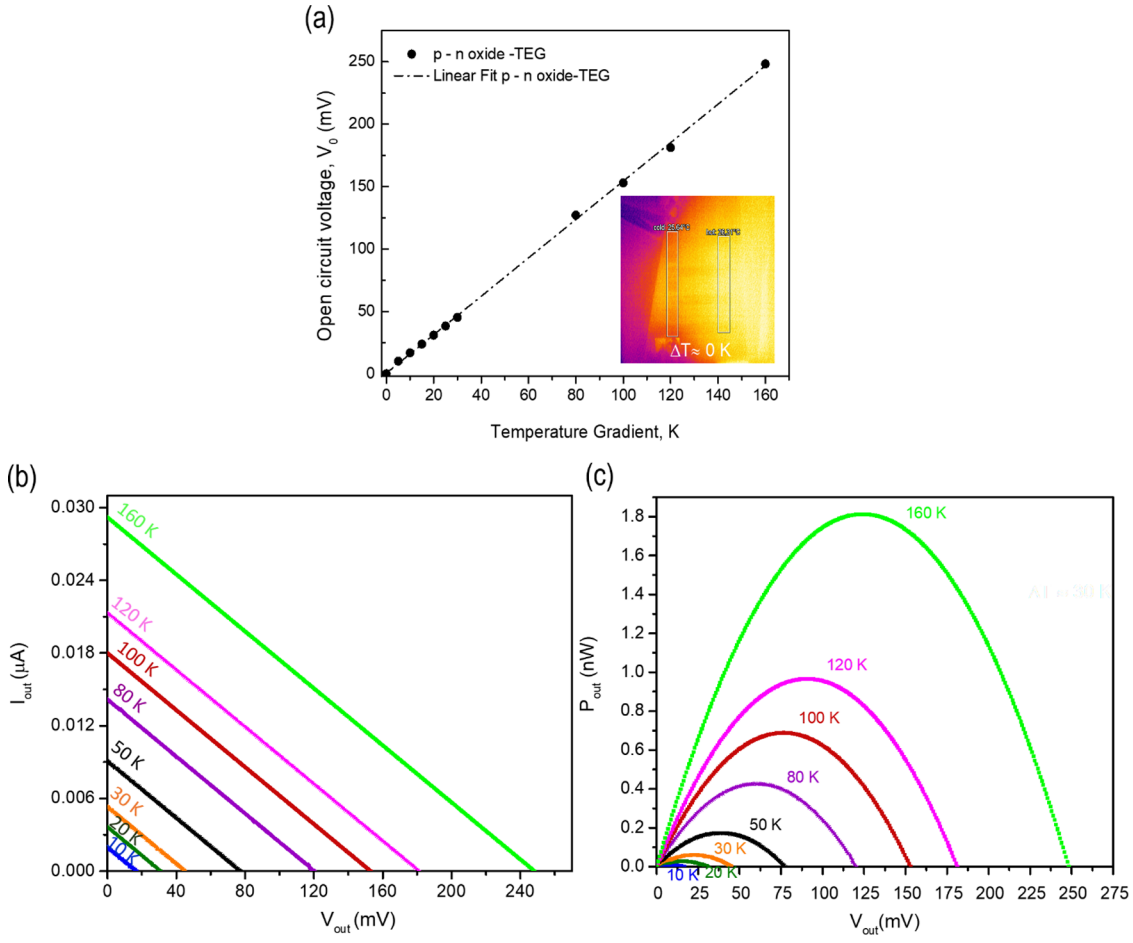

Figure 9. (a) Open-circuit voltage (V_0) of the four p−n TE pairs as a function of the temperature gradient between 10 and 160 K. The inset shows the thermography image of the p-SnO/n-ZnO device, showing the L-type design of the TEG and the (b) output current (I_{out}) and (c) output power (P_{out}) of the developed TEG as a function of output voltage (V_{out}) for different temperature gradients.

confirmed the presence of SnO and SnO_2 phases in the SnO_x films.[17,18] Moreover, the energy-dispersive X-ray spectroscopy (EDS) maps (Figure 6c) reveal the distribution of Zn, Sn, O, and Si elements in the layers and the substrate. The color image in RGB was obtained by superposition of images of each element and no perceptible diffusion between the layers is observed. It should be noted that the whole TEG structure was subjected to an annealing of 523 K during 3 h to promote the formation of SnO_x film (please see the Materials and Methods section), which confirms the stability of the p−n junction.

The presence of the p−n junction was investigated by the current−voltage (I−V) characteristics, at room temperature, in an indium tin oxide (ITO)/ZnO/SnO_x/ITO heterostructure. Figure S1 (available in the Supporting Information) shows the I−V curve for the ITO/ZnO/SnO_x/ITO heterostructure. A diode behavior was observed with a forward turn-on voltage of around 0.8 V and a forward-to-reverse current ratio of about 88 at 2 V. A similar behavior was also observed in other ZnO/SnO heterojunctions.[38]

The thermovoltage against ΔT is shown in Figure 7 for the ZnO and SnO_x films. A negative Seebeck coefficient of −120.8 ± 1.6 μV/K was obtained from the linear fitting for the ZnO film (Figure 7a), confirming the n-type conduction behavior (i.e., electrons are the majority carriers), while a p-type characteristic of SnO_x film is revealed by the positive Seebeck coefficient (α = +258.1 ± 7.3 μV/K; holes are the majority carriers) (Figure 7b). XPS results suggest that the SnO phase (52%) is dominant in the SnO_x film and therefore a p-type behavior is expected.[17] The Seebeck value for SnO_x films is approximately double the magnitude of that of the ZnO films.

Moreover, using the van der Pauw method, the electrical conductivity of 1.2×10^4 and 5.6×10^2 S/m for the ZnO and SnO_x films was determined, which results in a power factor of 180 ± 0.6 and 37 ± 2.8 μW/m K^2, respectively. Our ZnO power factor is higher than other ones reported for dense ZnO films, for example <35 μW/m K^2 for undoped and Dy-doped ZnO films[39] and ∼9 μW/m K^2 for nanowire-structured ZnO films (∼200 nm thick).[40] Moreover, our ZnO film shows a similar power factor at 298 K when compared with Al_2O_3/ZnO superlattices reported by Park et al.[10] Moreover, the achieved SnO_x power factor is higher than that of the tin oxide films produced by reactive sputtering recently reported by Jia et al.[41] with the power factor value of 11 μW/m K^2 and by SnO films reported by Miller et al,[42] with the power factor value of 1.2 μW/m K^2 at a low temperature of 325 K.

Thermal conductivity for both oxide films was recorded between 250 and 570 K (Figure 8). The thermal conductivities, k, of the ZnO and SnO_x films were determined to be 8.1−8.7 and 1.23−1.36 W/m K from 250 to 570 K, respectively. Particularly, the k values of ZnO and SnO_x films at 298 K of temperature are 8.7 and 1.24 W/m K, respectively. These values are comparable with the reported literature, in

https://doi.org/10.1021/acsami.1c09748
ACS Appl. Mater. Interfaces 2021, 13, 35187−35196

which it is possible to observe ZnO films with k values between 0.3 and 43 W/m K[43] and SnO_x films with k values between 0.2 and 2 W/m K.[42,44]

Considering the power factor and thermal conductivity measurements, the in-plane ZT values of ZnO and SnO_x thin films at 298 K were calculated. These were 1.6×10^{-3} and 4.5×10^{-5} for the ZnO and SnO_x, respectively, at 298 K.

The open-circuit voltage of the developed device, formed by four pairs of n-ZnO and p-SnO_x legs, was studied between 10 and 160 K, as shown in Figure 9. Our device reveals a maximum output voltage of 248 mV for 160 K. The device exhibit an overall thermoelectric Seebeck voltage of about 1.5 mV/K, which is in good agreement with the Seebeck coefficients of the individual p- and n-type materials, which suggests that an additional contribution to the generated electric power due to the separation of thermally excited charge carriers by the built-in field within the space-charge region of the junction is minimal.[45] A thermography image of the p−n device captured using an IR camera at the beginning of the measurements (with $\Delta T \approx 0$ K) is shown in the inset of Figure 9a. Moreover, the electric resistance of the device was measured to be 8.5 MΩ.

The power generation performance of the device was obtained by the measurements of the V_{out}/I_{out} (output voltage/output current) from 10 to 160 K, as shown in Figure 9b,c. The all-oxide p−n TEG generated the maximum power output of 1.8 nW (126 μW/cm^2) at ΔT = 160 K. Moreover, I_{out} and V_{out} that maximize the output power of the TEG are ≈0.0146 μA and ≈124 mV, respectively. It is noteworthy that the output power density at 30 K (≈8 μW/cm^2) is of the same magnitude as those of the hybrid Bi_2Te_3/PVA TE composites with films of thickness between 10 and 265 μm,[6] with the advantage of being thinner and composed by low-cost and eco-friendly materials. In addition, our all p−n device shows comparable output power values at ΔT = 30 K compared to the four pairs of Al_2O_3/ZnO superlattice film/p-$Bi_{0.5}Sb_{1.5}Te_3$ thermoelectric generator reported by Park et al.[10] Moreover, our device does not have metal contacts, making it more interesting for high-temperature applications, and can offer higher output voltages than the ones reported in ref 10 due to higher Seebeck coefficients of our oxide films.

CONCLUSIONS

In this work, a novel all-oxide p−n 2D thin-film TEG device concept was successfully designed using n-type ZnO and p-type SnO_x films. DFT calculations and XPS measurements suggest the formation of a type II heterojunction, while STEM and EDS of the p−n junction reveal a sharp interface between the SnO_x and ZnO layers, after an annealing procedure of 250 °C for 3 h, confirming the high quality of the p−n junction. Power factors of 180 and 37 μW/(m K^2) were obtained for n-type ZnO and p-type SnO_x, respectively. The thermal conductivity measurements for each oxide film suggest that the materials are stable up to temperatures of 575 K and the open-circuit voltage of the TEG device is in good agreement with the voltages Seebeck coefficients of the individual p- and n-type materials, which suggests that any additional contribution to the generated electric power due to the separation of thermally excited charge carriers by the built-in field within the space-charge region of the junction is minimal. Our device delivered a maximum output power (power density) of 1.8 nW (126 μW/cm^2) for a temperature difference of 160 K, with a large open-circuit voltage of 240 mV. The development of heterostructures based on n-type ZnO and p-type SnO_x thin films may be an effective way to develop a nontoxic all-oxide TEG device.

ASSOCIATED CONTENT

Supporting Information

The Supporting Information is available free of charge at https://pubs.acs.org/doi/10.1021/acsami.1c09748.

Current−voltage curve for the ITO/ZnO/SnO_x/ITO heterostructure (PDF)

AUTHOR INFORMATION

Corresponding Authors

Eliana M. F. Vieira − *CMEMS—UMINHO, Universidade do Minho, 4804-533 Guimaraes, Portugal;* orcid.org/0000-0001-8198-6024; Email: evieira@dei.uminho.pt

José P. B. Silva − *Centro de Física das Universidades do Minho e do Porto (CF-UM-UP, 4710-057 Braga, Portugal;* Email: josesilva@fisica.uminho.pt

Authors

Kateřina Veltruská − *Department of Surface and Plasma Science, Faculty of Mathematics and Physics, Charles University, 18000 Prague 8, Czech Republic*

Cosmin M. Istrate − *National Institute of Materials Physics, 077125 Magurele, Romania*

Veniero Lenzi − *Centro de Física das Universidades do Minho e do Porto (CF-UM-UP, 4710-057 Braga, Portugal;* orcid.org/0000-0002-3633-1966

Vanira Trifiletti − *School of Engineering and Materials Science, Queen Mary University of London, London E1 4NS, U.K.*

Bruno Lorenzi − *Department of Materials Science, University of Milano-Bicocca, I-20125 Milano, Italy*

Vladimír Matolín − *Department of Surface and Plasma Science, Faculty of Mathematics and Physics, Charles University, 18000 Prague 8, Czech Republic*

Corneliu Ghica − *National Institute of Materials Physics, 077125 Magurele, Romania*

Luis Marques − *Centro de Física das Universidades do Minho e do Porto (CF-UM-UP, 4710-057 Braga, Portugal*

Oliver Fenwick − *School of Engineering and Materials Science, Queen Mary University of London, London E1 4NS, U.K.;* orcid.org/0000-0001-7499-5117

Luis M. Goncalves − *CMEMS—UMINHO, Universidade do Minho, 4804-533 Guimaraes, Portugal*

Complete contact information is available at: https://pubs.acs.org/10.1021/acsami.1c09748

Author Contributions

E.M.F.V. and J.P.B.S. contributed equally to this work. E.M.F.V. and J.P.B.S. conducted thin films and device fabrication, characterization, and data analysis. K.V. and V.M. made XPS measurements and analysis. C.M.I. and C.G. made STEM measurements and characterization. V.L. and L.M. performed the DFT calculations and analysis. V.T. and O.F. performed the thermal conductivity measurements and analysis. B.L. performed the electrical measurements and analysis. L.M.G. conceived and designed the experiments. E.M.F.V. wrote the manuscript. The authors contributed equally in discussing the results and the manuscript.

https://doi.org/10.1021/acsami.1c09748
ACS Appl. Mater. Interfaces 2021, 13, 35187−35196

Notes

The authors declare no competing financial interest.

■ ACKNOWLEDGMENTS

This work was supported by the FCT national funds, under the national support to R&D units grant, through (i) the reference project UIDB/04436/2020 and UIDP/04436/2020, (ii) the Portuguese Foundation for Science and Technology (FCT) in the framework of the Strategic Funding Contracts UIDB/04650/2020; V.T. is funded by an MSCA Individual Fellowship (HYPERTHERM 798271); O.F. is supported by a Royal Society University Research Fellowship (UF140372). Part of this work was supported by the COST Action CA18203, Optimizing Design for Inspection (ODIN), and the project PTDC/EEI-TEL/29670/2017 (POCI-01-0145-FEDER-029670), co-financed by the European Regional Development Fund (ERDF), through COMPETE 2020. The authors acknowledge the CERIC-ERIC Consortium for access to experimental facilities and financial support under proposal 20192056. The authors thank engineers José Santos and Nuno Gomes for technical support at the Thin Film Laboratories.

■ REFERENCES

(1) Strasser, M.; Aigner, R.; Lauterbach, C.; Sturm, T. F.; Franosch, M.; Wachutka, G. Micromachined CMOS thermoelectric generators as on-chip power supply. *Sens. Actuators, A* **2004**, *114*, 362−370.

(2) Rowe, D. M. *CRC Handbook of Thermoelectrics*, 1st ed.; CRC Press, 1995.

(3) Shi, X.-L.; Zou, J.; Chen, Z.-G. Advanced Thermoelectric Design: From Materials and Structures to Devices. *Chem. Rev.* **2020**, *120*, 7399−7515.

(4) Jaziri, N.; Boughamoura, A.; Müller, J.; Mezghani, B.; Tounsi, F.; Ismail, M. A comprehensive review of Thermoelectric Generators: Technologies and common applications. *Energy Rep.* **2020**, *6*, 264−287.

(5) Vieira, E. M. F.; Pires, A. L.; Silva, J. P. B.; Magalhães, V. H.; Grilo, J.; Brito, F. P.; Silva, M. F.; Pereira, A. M.; Goncalves, L. M. High-Performance μ-Thermoelectric Device Based on Bi_2Te_3 /Sb_2Te_3 p−n Junctions. *ACS Appl. Mater. Interfaces* **2019**, *11*, 38946−38954.

(6) Pires, A. L.; Cruz, I. F.; Silva, J.; Oliveira, G. N. P.; Ferreira-Teixeira, S.; Lopes, A. M. L.; Araújo, J. P.; Fonseca, J.; Pereira, C.; Pereira, A. M. Printed Flexible μ-Thermoelectric Device Based on Hybrid Bi_2Te_3 /PVA Composites. *ACS Appl. Mater. Interfaces* **2019**, *11*, 8969−8981.

(7) Teo, A. J. T.; Mishra, A.; Park, I.; Kim, Y.-J.; Park, W.-T.; Yoon, Y.-J. Polymeric Biomaterials for Medical Implants and Devices. *ACS Biomater. Sci. Eng.* **2016**, *2*, 454−472.

(8) Meng, Q.; Jiang, Q.; Cai, K.; Chen, L. Preparation and thermoelectric properties of PEDOT:PSS coated Te nanorod/PEDOT:PSS composite films. *Org. Electron.* **2019**, *64*, 79−85.

(9) Lu, Y.; Ding, Y.; Qiu, Y.; Cai, K.; Yao, Q.; Song, H.; Tong, L.; He, J.; Chen, L. Good Performance and Flexible PEDOT:PSS/Cu_2Se Nanowire Thermoelectric Composite Films. *ACS Appl. Mater. Interfaces* **2019**, *11*, 12819−12829.

(10) Park, N.-W.; Ahn, J.-Y.; Park, T.-H.; Lee, J.-H.; Lee, W.-Y.; Cho, K.; Yoon, Y.-G.; Choi, C.-J.; Park, J.-S.; Lee, S.-K. Control of phonon transport by the formation of the Al_2O_3 interlayer in Al_2O_3 − ZnO superlattice thin films and their in-plane thermoelectric energy generator performance. *Nanoscale* **2017**, *9*, 7027−7036.

(11) Matsubara, I.; Funahashi, R.; Takeuchi, T.; Sodeoka, S.; Shimizu, T.; Ueno, K. Fabrication of an all-oxide thermoelectric power generator. *Appl. Phys. Lett.* **2001**, *78*, 3627−3629.

(12) New Atlas, Wearable Thermoelectric Generator Could Extend Your Smartwatch's Battery Life, 2014. http://www.gizmag.com/wearable-thermoelectric-generator/31617 (accessed May 21, 2021).

(13) Yang, Y.; Wei, X.-J.; Liu, J. Suitability of a thermoelectric power generator for implantable medical electronic devices. *J. Phys. D. Appl. Phys.* **2007**, *40*, 5790−5800.

(14) Thermo Life, White Paper, 2021. Available at: http://www.poweredbythermolife.com/whitepaper.htm (accessed May 21, 2021).

(15) Yang, F.; Zheng, S.; Wang, H.; Chu, W.; Dong, Y. A thin film thermoelectric device fabricated by a self-aligned shadow mask method. *J. Micromech. Microeng.* **2017**, *27*, No. 055005.

(16) Zhou, C.; Ghods, A.; Yunghans, K. L.; Saravade, V. G.; Patel, P. V.; Jiang, X.; Kucukgok, B.; Lu, N.; Ferguson, I. *ZnO for Solar Cell and Thermoelectric Applications*, Proceedings of SPIE, Oxide-Based Materials and Devices VIII; International Society for Optics and Photonics: San Francisco, California, 2017; Vol. *101051*.

(17) Vieira, E. M. F.; Silva, J. P. B.; Veltruská, K.; Matolín, V.; Pires, A. L.; Pereira, A. M.; Gomes, M. J. M.; Goncalves, L. M. Highly sensitive thermoelectric touch sensor based on p-type SnO_x thin film. *Nanotechnology* **2019**, *30*, No. 435502.

(18) Silva, J. P. B.; Vieira, E. M. F.; Silva, J. M. B.; Gwozdz, K.; Figueiras, F. G.; Veltruská, K.; Matolín, V.; Istrate, M. C.; Ghica, C.; Sekhar, K. C.; Kholkin, A. L.; Goncalves, L. M.; Chahboun, A.; Pereira, M. Perovskite ferroelectric thin film as an efficient interface to enhance the photovoltaic characteristics of Si/SnO x heterojunctions. *J. Mater. Chem. A* **2020**, *8*, 11314−11326.

(19) Valalaki, K.; Benech, P.; Galiouna Nassiopoulou, A. High Seebeck Coefficient of Porous Silicon: Study of the Porosity Dependence. *Nanoscale Res. Lett.* **2016**, *11*, No. 201.

(20) Linseis, V.; Völklein, F.; Reith, H.; Nielsch, K.; Woias, P. Advanced platform for the in-plane ZT measurement of thin films. *Rev. Sci. Instrum.* **2018**, *89*, No. 015110.

(21) Völklein, F.; Reith, H.; Meier, A. Measuring methods for the investigation of in-plane and cross-plane thermal conductivity of thin films. *Phys. Status Solidi A* **2013**, *210*, 106−118.

(22) Liu, T.; Zhao, X.; Li, J.; Liu, Z.; Liscio, F.; Milita, S.; Schroeder, B. C.; Fenwick, O. Enhanced control of self-doping in halide perovskites for improved thermoelectric performance. *Nat. Commun.* **2019**, *10*, No. 5750.

(23) Kresse, G.; Furthmüller, J. Efficient iterative schemes for ab initio total-energy calculations using a plane-wave basis set. *Phys. Rev. B* **1996**, *54*, 11169−11186.

(24) Kresse, G.; Joubert, D. From ultrasoft pseudopotentials to the projector augmented-wave method. *Phys. Rev. B* **1999**, *59*, 1758−1775.

(25) Blöchl, P. E. Projector augmented-wave method. *Phys. Rev. B* **1994**, *50*, 17953−17979.

(26) Perdew, J. P.; Burke, K.; Ernzerhof, M. Generalized Gradient Approximation Made Simple. *Phys. Rev. Lett.* **1996**, *77*, 3865−3868.

(27) Hinuma, Y.; Oba, F.; Kumagai, Y.; Tanaka, I. Band offsets of $CuInSe_2$/CdS and CuInSe2/ ZnS (110) interfaces: A hybrid density functional theory study. *Phys. Rev. B* **2013**, *88*, No. 035305.

(28) Hinuma, Y.; Grüneis, A.; Kresse, G.; Oba, F. Band alignment of semiconductors from density-functional theory and many-body perturbation theory. *Phys. Rev. B* **2014**, *90*, No. 155405.

(29) Onida, G.; Reining, L.; Rubio, A. Electronic excitations: density-functional versus many-body Green's-function approaches. *Rev. Mod. Phys.* **2002**, *74*, 601−659.

(30) Starke, R.; Kresse, G. Self-consistent Green function equations and the hierarchy of approximations for the four-point propagator. *Phys. Rev. B* **2012**, *85*, No. 075119.

(31) Klimeš, J.; Kaltak, M.; Kresse, G. Predictive *GW* calculations using plane waves and pseudopotentials. *Phys. Rev. B* **2014**, *90*, No. 075125.

(32) Srikant, V.; Clarke, D. R. On the optical band gap of zinc oxide. *J. Appl. Phys.* **1998**, *83*, 5447−5451.

(33) Ganose, A. M.; Scanlon, D. O. Band gap and work function tailoring of SnO_2 for improved transparent conducting ability in photovoltaics. *J. Mater. Chem. C* **2016**, *4*, 1467−1475.

(34) Saji, K. J.; Venkata Subbaiah, Y. P.; Tian, K.; Tiwari, A. P-type SnO thin films and SnO/ZnO heterostructures for all-oxide electronic

https://doi.org/10.1021/acsami.1c09748
ACS Appl. Mater. Interfaces 2021, 13, 35187−35196

and optoelectronic device applications. *Thin Solid Films* **2016**, *605*, 193−201.
(35) Quackenbush, N. F.; Allen, J. P.; Scanlon, D. O.; Sallis, S.; Hewlett, J. A.; Nandur, A. S.; Chen, B.; Smith, K. E.; Weiland, C.; Fischer, D. A.; Woicik, J. C.; White, B. E.; Watson, G. W.; Piper, L. F. J. Origin of the Bipolar Doping Behavior of SnO from X-ray Spectroscopy and Density Functional Theory. *Chem. Mater.* **2013**, *25*, 3114−3123.
(36) Wang, S.; Tian, H.; Ren, C.; Yu, J.; Sun, M. Electronic and optical properties of heterostructures based on transition metal dichalcogenides and graphene-like zinc oxide. *Sci. Rep.* **2018**, *8*, No. 12009.
(37) Silva, J. P. B.; Vorokhta, M.; Dvořák, F.; Sekhar, K. C.; Matolín, V.; Moreira, J. A.; Pereira, M.; Gomes, M. J. M. Unraveling the resistive switching effect in ZnO/0.5Ba($Zr_{0.2}Ti_{0.8}$)O_3 -0.5($Ba_{0.7}Ca_{0.3}$)-TiO_3 heterostructures. *Appl. Surf. Sci.* **2017**, *400*, 453−460.
(38) Javaid, K.; Xie, Y. F.; Luo, H.; Wang, M.; Zhang, H. L.; Gao, J. H.; Zhuge, F.; Liang, L. Y.; Cao, H. T. The electrical properties of n-ZnO/p-SnO heterojunction diodes. *Appl. Phys. Lett.* **2016**, *109*, No. 123507.
(39) Paulson, A.; Muhammed Sabeer, N. A.; Pradyumnan, P. P. Enhancement of optical and thermoelectric properties in dysprosium doped ZnO thin films as an impact of non-parabolic band structure. *Mater. Sci. Eng. B* **2020**, *262*, No. 114745.
(40) Liu, S.; Li, G.; Xiao, L.; Jia, B.; Gao, Y.; Wang, Q. Effect of morphology evolution on the thermoelectric properties of oxidized ZnO thin films. *Appl. Surf. Sci.* **2018**, *436*, 354−361.
(41) Jia, J.; Sugane, T.; Nakamura, S.; Shigesato, Y. *p*-type conduction mechanism in continuously varied non-stoichimetric SnO_x thin films deposited by reactive sputtering with the impedance control. *J. Appl. Phys.* **2020**, *127*, No. 185703.
(42) Miller, S. A.; Gorai, P.; Aydemir, U.; Mason, T. O.; Stevanović, V.; Toberer, E. S.; Snyder, G. J. SnO as a potential oxide thermoelectric candidate. *J. Mater. Chem. C* **2017**, *5*, 8854−8861.
(43) Kaźmierczak-Bałata, A.; Bodzenta, J.; Guziewicz, M. Microscopic investigations of morphology and thermal properties of ZnO thin films grown by atomic layer deposition method. *Ultramicroscopy* **2020**, *210*, No. 112923.
(44) Mohamed, R.; Syed Mustafa, S. A.; Norizan, M. N.; Suraya Amerudin, L. Thermal conductivity and tensile properties of tin oxide filled UPR/EPS composites with and without organic nanocrystal. *IOP Conf. Ser.: Mater. Sci. Eng.* **2017**, *223*, No. 012029.
(45) Maculewicz, F.; Wagner, T.; Arzi, K.; Hartmann, N.; Weimann, N.; Schmechel, R. Experimental evidence for the separation of thermally excited bipolar charge carries within a p-n junction: A new approach to thermoelectric materials and generators. *J. Appl. Phys.* **2019**, *125*, No. 184502.
(46) Shin, W.; Murayama, N.; Ikeda, K.; Sago, S. Thermoelectric power generation using Li-doped NiO and (Ba, Sr)PbO3 module. *J. Power Sources* **2001**, *103*, 80−85.
(47) Park, K.; Lee, G. W. Fabrication and thermoelectric power of π-shaped Ca3Co4O9/CaMnO3 modules for renewable energy conversion. *Energy* **2013**, *60*, 87−93.
(48) Zappa, D.; Dalola, S.; Faglia, G.; Comini, E.; Ferroni, M.; Soldano, C.; Ferrari, V.; Sberveglieri, G. Integration of ZnO and CuO nanowires into a thermoelectric module. *Beilstein J. Nanotechnol.* **2014**, *5*, 927−936.
(49) Kanas, N.; Bittner, M.; Desissa, T. D.; Singh, S. P.; Norby, T.; Feldhoff, A.; Grande, T.; Wiik, K.; Einarsrud, M.-A. All-Oxide Thermoelectric Module with in Situ Formed Non-Rectifying Complex p−p−n Junction and Transverse Thermoelectric Effect. *ACS Omega* **2018**, *3*, 9899−9906.
(50) Caliari, F. R.; Lee, H.; Sampath, S. Optimization of All-Oxide 2D Layered Thermoelectric Device Fabricated by Plasma Spray. *J. Therm. Spray Technol.* **2020**, *29*, 1815−1826.
(51) Kanas, N.; Bjørk, R.; Wells, K. H.; Schuler, R.; Einarsrud, M.-A.; Pryds, N.; Wiik, K. Time-Enhanced Performance of Oxide Thermoelectric Modules Based on a Hybrid p−n Junction. *ACS Omega* **2021**, *6*, 197−205.

https://doi.org/10.1021/acsami.1c09748
ACS Appl. Mater. Interfaces 2021, 13, 35187−35196